Research article

Combined role of molybdenum and nitrogen in Limiting corrosion and pitting of super austenitic stainless steel

Bingbing Li [a], Yuping Lang [a,*], Haitao Chen [a], Hanqiu Feng [a], Huapeng Qu [a], Xu Sun [b], Zhiling Tian [a]

[a] *Central Iron and Steel Research Institute Company Limited, Beijing, 100081, China*
[b] *Material Digital R&D Center, China Iron & Steel Research Institute Group, Beijing, 100081, China*

A R T I C L E   I N F O

A B S T R A C T

The molybdenum and nitrogen content of super austenitic stainless steel in Cl^- solution is shown to influence pitting resistance using immersion, electrochemical testing, and simulation. Variations in Mo and N content affect the defect density, resistance, and densification of the passive film, thereby reducing the number of pitting. A higher local pH associated with the pitting pits and an increase in $NH_3(NH_4^+)$ are the results of increased N content, which also slows the rate of pitting expansion. The combined effects of fewer actively reactive spots within the passive film retarded pitting, and decreased corrosion rates due to $NH_3(NH_4^+)$ mitigation of local acidity which serves to reduce the corrosion rate. The work function is improved to a greater extent when Mo and N are co-doped compared with individual Mo and N doping, and the adsorption energy is significantly increased when Mo and N are co-doped, indicating a synergistic role for Mo and N in the prevention of corrosion by Cl^-.

1. Introduction

Due to its exceptional corrosion resistance of super austenitic stainless steel (SASS), it is frequently utilized in industries with harsh environments [1–3]. The development of a passive coating on the surface of SASS is the main factor underlying its corrosion resistance. By minimizing or even completely isolating the corrosive medium from the stainless steel surface, this passive coating functions as a barrier to prevent corrosion [4–6]. To evaluate the local corrosion resistance of SASS, the pitting resistance equivalent number (PREN) is commonly used. The PREN is calculated using various formulas, but the most widely used takes the form, PREN=Cr(wt.%) + 3.3 × Mo(wt.%) + 16 × N(wt.%) [7]. This equation demonstrates that the sum of the elements chromium, molybdenum, and nitrogen with their correlation coefficients determines the resistance to pitting corrosion. However, these alloying materials interact in a manner that goes beyond simple addition, and the overall impact of these interactions can be complex.

According to Nagarajan and Rajendran [8], Mo and N can promote passivation, creating a more stable passive coating that permits faster passivation and eventually improves corrosion resistance by lowering peak current density transients. According to Olsson [9] and Lu [10] et al., nitrogen dissolution produces NH_3 and NH_4^+, which serve as excellent pH buffers and promote the formation of a passive film. According to Clayton et al. [11], Mo participates in the deprotonation of hydroxides, which results in oxygen abundance inside the passive film and free protons, helping to generate ammonia ions. According to Ives [12] et al., nitrogen can create

---

ammonium compounds that can bind to reactive oxidants like free chlorine or bromine to create lower reactive chloramines as well as bromamines, preventing the growth of pitting pits.

To establish how Mo and N affect the synergistic effect of pitting corrosion, we have first applied PREN as a basis for assessment and modified the Mo and N content accordingly. We have used immersion tests to determine the effect of Mo and N, electrochemical analysis to determine the properties of the passive film of SASS, along with XPS and TEM to identify the components and depth of the passive film. Furthermore, simulations uncovered synergistic effects of molybdenum and nitrogen in the passive film. We have investigated the passive film Cl^- resistance additive effect. The mechanism of Mo–N synergy in the Cl^- ion pitting corrosion resistance of SASS is clarified in this work.

2. Experimental

2.1. Material preparation

In a vacuum induction furnace, pure metals and alloying components were combined based on the composition design plan. After the vacuum was broken, ferrochrome nitride and Ni–Mg deoxidation were combined. The alloy was cast, air hammer forged at 1130–1160 °C into 40 mm slabs, and hot-rolled at 1160 °C to produce 5 mm sheets. Table 1 provides the composition of the specimens. Hot rolled samples were maintained at 1200 °C for 2 h, then rapidly water-cooled to produce an austenitic structure.

2.2. Methodology for the study of pitting pits

Samples (30 mm × 20 mm × 2 mm) were cleaned using an ultrasonic cleaner and rapidly desiccated. Following 24 h of sample resting, the samples were accurately weighed, and the surface area was measured before immersion in a 6% $FeCl_3$ + 0.05 mol/L HCl solution at 75 °C for 12 h. The surface solution frozen body was then removed, employing the liquid nitrogen flash freezing technique [13]. To generate a larger number of pitting pit solutions, 30 similar samples were taken. The frozen body of the pitting pit solution from the 30 samples was collected and quantified by applying the absorption method, following ASTM D1426-93 and ASTM D3867-90 for the analysis of amino nitrogen (NH_3–N) and nitrogen-based nitrogen (NO_3–N) [14]. After extracting the sample solution from the pitting pit, washing it with distilled water, and vibrating it with alcohol, the sample was blow-dried. The Bruker ContourX-500 and Vision64 software were used to assess the three-dimensional morphology of the corrosion pits; According to GB/T 17897-2016 to calculate the corrosion rate [g/(m^2•h)].

2.3. Electrochemical testing

The electrochemical tests were carried out using a typical three-electrode system. It included a polished working electrode with an exposed surface area of 1 cm^2, a saturated calomel electrode as the reference electrode, and a platinum sheet as the counter electrode. The solution was deoxygenated by venting nitrogen for 20 min before the measurements, and any surface oxide film was removed by cathodically pre-polarizing the working electrode with a −800 mV (vs. SCE) at 600 s. Nitrogen gas was constantly bubbled into the solution during the entire experiment with a speed of 0.5 L/min.

Immersion method and cyclic polarization tests were carried out at 75 °C with a sweep speed of 20 mV/min containing 6% $FeCl_3$ + 0.05 mol/L HCl [15]. Reverse the scanning direction when the current reaches 1 mA.

Potentiodynamic polarization was monitored over a period of −600 mV–1000 mV (vs. SCE) in a 3.5% NaCl solution at 50 °C with a sweep speed of 20 mV/min. Potentiostatic tests at 50 °C for 1 h at 300 mV (vs. SCE).

The impedance and semiconductor properties of the passive films were investigated using electrochemical impedance spectroscopy (EIS) and Mott Schottky (M − S), respectively. Applying a frequency sweep in the opposite direction between 10^5 Hz and 10^{-2} Hz and an amplitude of 5 mV, the EIS was fitted using the Zsim software. The M − S utilized a voltage range of 1 to −0.5 V and a potential sweep of 50 mV/s at a frequency of 2 kHz in the negative direction.

2.4. Determination of passive film morphology and composition

A GATAN PIPS II 695 precision ion thinning device was used to generate the TEM samples. Passive films can be produced within seconds [16] due to the strong chromium, molybdenum, and nitrogen concentrations of the test steel. To ensure a precise and consistent passive film thickness, some samples were subjected to TEM analysis (FEI Tacnai F20 transmission electron microscope) following preparation to assess the original passive film. Furthermore, the passive film was examined by TEM test after submerging some samples in a 3.5% NaCl solution at 50 °C for 24 h.

Table 1
Composition of the specimens/wt.%.

Sample	C	Si	Mn	Ni	Cr	Mo	N	Fe	PREN
Mo2N1	0.0062	0.33	0.39	24.35	26.39	4.52	0.29	Bal.	45.95
Mo1N1	0.0061	0.34	0.43	24.41	26.37	3.99	0.40	Bal.	45.94
Mo1N2	0.0065	0.33	0.42	24.37	26.33	3.48	0.51	Bal.	45.97

The Pourbaix diagram of Fe–Mo–N alloys in solution with 50 °C was calculated using Factasge to identify potential compounds in the passive films formed at 300 mV (vs. SCE). Following the potentiostatic tests, X-ray photoelectron spectroscopy (XPS) was performed to determine the chemical character and valence states of the passive films. The C 1s peak (at 284.8 eV), was applied to adjust the photoelectron peak binding energies, employing monochromatic Al Kα rays with a voltage of 1486.6 eV, power (150 W), take-off angle (45°), 700 μm × 300 μm analysis area, and sputtering rate of 3 nm/min with SiO_2 as a standard. Shirley-type and XPS peak version 4.1 were used to carry out sub-peak fitting and background removal modifications, respectively.
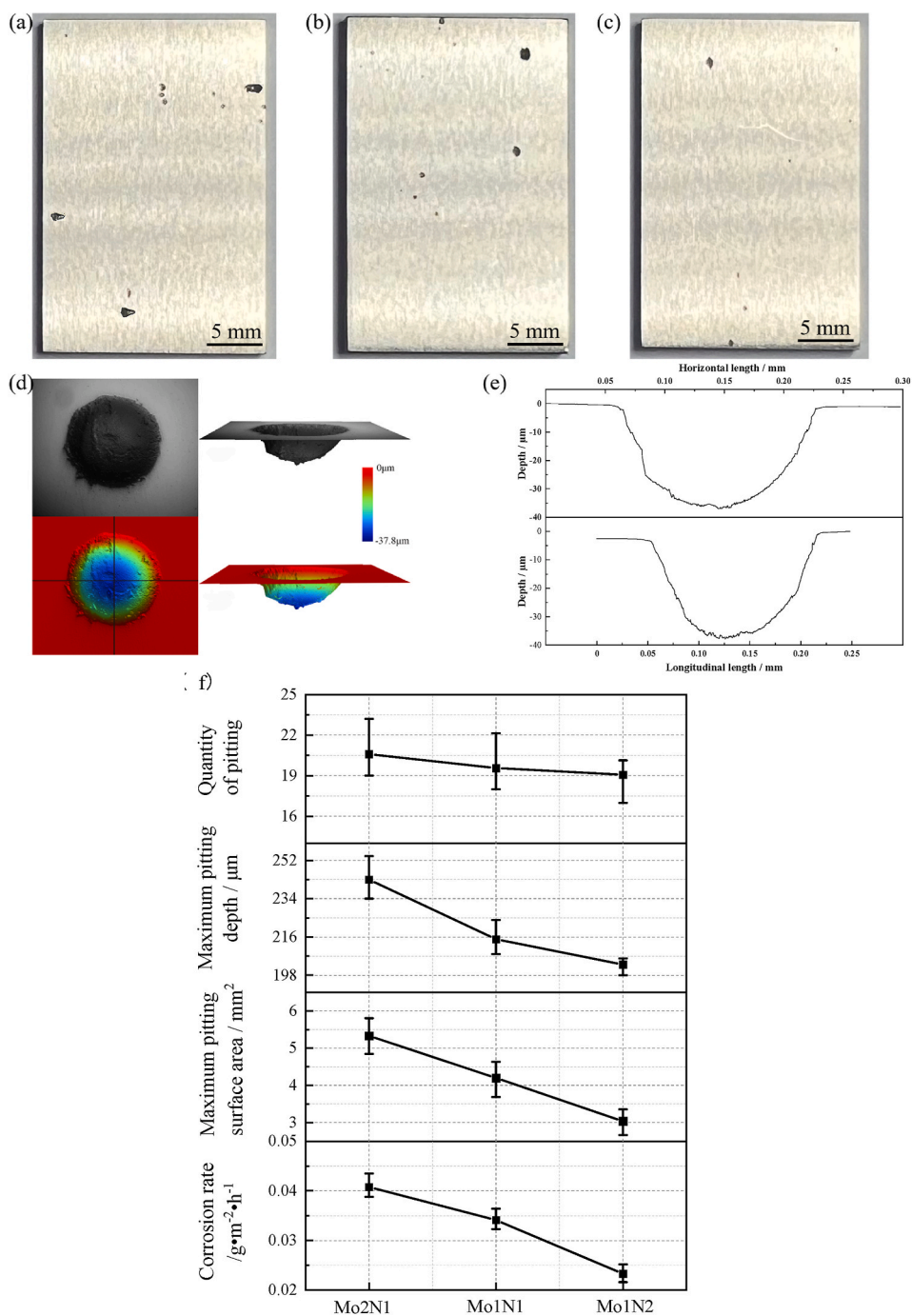

Fig. 1. Corrosion data after specimen immersion. (a) Mo2N1; (b) Mo1N1; (c) Mo1N2; (d) Three-dimensional view of pitting pits; (e) Pitting pit data; (f) Erosion data.

2.5. Methodology for NaCl adsorption simulation

The calculation of the adsorption energy employed one NaCl molecule to preserve the ionic character of Cl^-. The fabrication of Mo and N-doped Fe_2O_3 surfaces and analysis of NaCl adsorption behavior facilitated an understanding of the mechanism of passive films against Cl^- corrosion. Calculation of the spin-polarised DFT utilized Vienna Analogue Software Package (VASP) [17].

Exchange correlations among electrons were characterized using the generalized gradient approximation (GGA) of the Perdew-Burke Ernzerhof (PBE) [18], while d-orbital electrons' in situ Coulombic interactions were corrected using the GGA + U method with Hubbard U corrections of 4 eV and 5.5 eV for iron and molybdenum [19–22]. The plane wave cut-off energy for all calculations was set at 450 eV, with 10^{-5} eV serving as the energy convergence criterion and the surface and bulk model Brillouin zones were $4 \times 4 \times 1$ and $4 \times 4 \times 3$, respectively [23].

Atoms in the top 8 layers were free until the applied force was reduced to below 0.02 eV/A for each atom, whereas the bottom 10 atomic layers remained stationary. The distance (0001) above the upper 15 Å is a vacuum layer, and the antiferromagnetic order among the Fe atomic layers in Fe_2O_3 was + + - -. Bader charge analysis was performed to determine the surface atomic charge [24,25]. A dipole correction was made for the work function calculation as the asymmetric upper and lower surface differing electronegativity resulted in an additional dipole moment in the a-direction, leading to an incorrectly calculated vacuum electrostatic potential [26].

3. Results and discussion

3.1. Effect of Mo and N concentration on pitting

In Fig. 1(a–c), the pitting was observed at the sample surface post-immersion and exhibited a circular-like shape for small pits, whereas the larger pits displayed irregular shapes. Fig. 1(d) and (e) show the three-dimensional morphology of a representative small pitting pit, characterized by open circles with a radius greater than the pitting pit depth direction, and no evidence of self-sealing water droplet corrosion pits. This may be due to the fact that N prevents the generation of autocatalysis in the pitting pits, or it may be caused by the comparatively low duration of the corrosion.

The immersion corrosion data of the samples are shown in Fig. 1(f). All the corrosion data decreases with increasing N concentration decreases with decreasing Mo concentration, demonstrating the enhanced corrosion resistance of the test steel.

With higher N levels and smaller Mo levels, the quantity of pitting pits decreases accordingly, which may be ascribed to the change in the composition and structure of the passive film. The shift in alloy components resulted in changes in the passive film, so that fewer surface defects, a decline in active pitting corrosion sites, and delayed initiation of pitting corrosion under the same environmental conditions.

Furthermore, the increase in N content coupled with a decrease in Mo content leads to a reduction in the maximum area and maximum depth of pitting. It is due to the decreased propagation rate of pitting pits, resulting in accelerated re-passivation or delayed initiation of pitting corrosion. To better understand the root reasons, a cyclic polarization test was conducted.

Fig. 2 illustrates the cyclic polarization of the specimens in a 6% $FeCl_3$ + 0.05 mol/L solution at 75 °C. The anodic polarization curve has no active-passive transition, which is consistent with transient passivation [27]. With an increase in the N content of the test steels up to 0.51 wt% and a decrease in Mo content to 3.48 wt%, several changes were observed. The critical current density decreased, while the self-corrosion and pitting potentials exhibited a slight increase. These observations indicate that greater N content and less Mo content contributed to a decreased potential for pitting pit initiation. The phenomenon is related to changes in the component and structure of the passive film, as discussed below.

Noticeable current swings were observed in all passive regions, indicating the presence of a large number of sub-stable pitting pits. With higher N concentrations and lower Mo concentrations, these current fluctuations were initially observed at higher potentials,
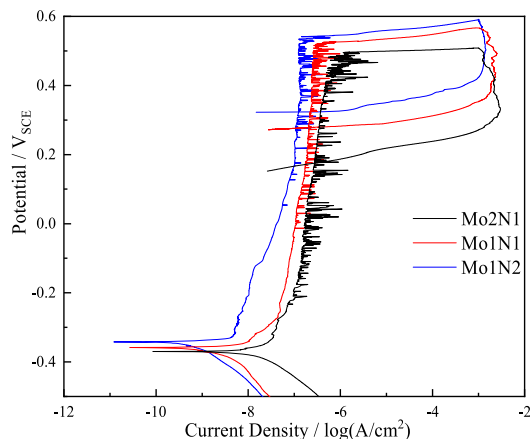

Fig. 2. Cyclic polarization curves in 6 % $FeCl_3$+0.05 mol/L solution at 75 °C.

with a lower frequency and a reduced transient current amplitude. It indicates content variations hindered the formation of sub-stable pitting pits. This finding agrees with the results of the immersion corrosion tests.

When reversing the potential after reaching 1 mA, the current density exhibited a peak and a subsequent decrease, despite the decrease in applied potential. This behavior resulted in a hysteresis loop, signifying the presence of a retardation in re-passivation [28]. Noticeable rise in re-passivation potential was observed, suggesting that higher N level and lower Mo level enhanced the sensitivity of the re-passivate with significant inhibition of the pitting pit propagation rate. In addition, the gap by which the pitting and the re-passivation potential gradually diminished, signifying a reinforcement of re-passivation kinetics [29]. The area of the hysteresis loop is a direct measure of the pit propagation kinetics [30]. Increasing N concentration and decreasing Mo concentration resulted in a gradual reduction in the hysteresis loop area, suggesting an inhibition in the rate of pitting pit propagation. This can be attributed to the generation of NH_4^+ from N, which alleviates the local pH. A higher N content generates a greater amount of NH_4^+, leading to a faster reduction in the pitting pit propagation rate. The pitting pit solution was analyzed, and NH_3 (NH_4^+) and NO_3 content are given in Table 2. It is clear that the presence of NO_3 in this experiment is minimal, and the majority of the nitrogen (N) is in the form of NH_3 (NH_4^+), which lowers the pitting expansion rate and maximum pitting depth, raising the local pH which relieves local acidification.

3.2. Effect of N and Mo content on polarization

As the N content rises and the Mo content falls, the passive film composition and structure can change, which may be the reason for fewer pitting pits. A thorough analysis of the passive film was conducted as the reduction in the maximum area and depth of pitting may also be caused by a delay in the initiation of the pitting corrosion as the N content rises and the Mo content falls.

Fig. 3(a) displays the dynamic potential polarization for the samples in a 3.5% NaCl solution at 50 °C. A significant passive zone is evident for all three samples up to the *trans*-passive disintegration. The passive current density and critical current density decreased as the N content of the test steels increased to 0.51 wt% and the Mo content fell to 3.48 wt%, while the self-corrosion potential gradually increased, suggesting that the influence of the N and Mo content on the corrosion resistance are synergistic and not just additive in terms of PREN.

A potential of 300 mV (vs. SCE) for 60 min produces a passive film. Fig. 3(b) shows the transient current densities of the samples in a 3.5% NaCl solution at 50 °C. In Fig. 3(b), it is observed that the current density of the samples quickly reduced, which is explained by the cathodic pre-polarization with −800 mV (vs. SCE) for 600 s before the test that served to remove the passive film. The dissolution rate was much lower than the speed of passive film formation upon application of a 300 mV (vs. SCE) potential, which facilitated the development of the passive film [31–34]. The current density maintains relative stability over time. The three sample surfaces are completely passivated and appear to be relatively stable, according to the enlarged section of Fig. 3(b). The passive film current density was reduced with increasing N and decreasing Mo content, indicating a greater protective effect [35], which may be caused by the change in film composition as a result of the varying Mo and N content.

3.3. Effect of N and Mo content on passive film impedance

The EIS results for the three samples are shown in Fig. 4, following 60 min of steady potential polarization at 300 mV (vs. SCE) in a 3.5% NaCl solution at 50 °C. When the Kramers-Kronig (K–K) transformation (real axis translated to imaginary axis and imaginary axis transformed to real axis) was applied to the experimental values, the variance of each EIS data curve fit was less than 10^{-3}, demonstrating the effectiveness of the EIS values [36,37].

The Bode plots (Fig. 4(b)), where the phase angle is approaching 90°, demonstrate that the capacitive properties of the three samples diverge from the ideal capacitive properties, it can be represented by a constant phase element (CPE) [38,39]. The Nyquist plots (Fig. 4(a)) are all curved, demonstrating that the three samples possess comparable impedance properties under ambient conditions. The definition of the impedance of the CPE is eq. (1):

$$Z_{CPE} = 1/Q(j\omega)^n \tag{1}$$

where Q, ω, $j^2 = -1$, n are, respectively, the fitting parameters, angular frequency (rad/s), imaginary number, and CPE exponent. An exponent (n) value of 1 for CPE indicates ideal capacitance, n = 0 indicates resistance, and n = 0.5 indicates Warburg impedance; n varies with the degree of coarseness of the passive film [40].

An equivalent circuit model was fitted to the measurement values. The equivalent circuit is illustrated in Fig. 5, where R_S and R represent the solution resistance and passive film resistance, respectively.

The values replicated for the equivalent circuit parts are shown in Table 3, where χ^2, the variance of the fitted values concerning the experimental data, is less than 10^{-3}, indicating an accurate fit. The n and R levels increase with growing N content and falling Mo

Table 2
Content of NH_3 (NH_4^+) and NO_3 in pitting pits.

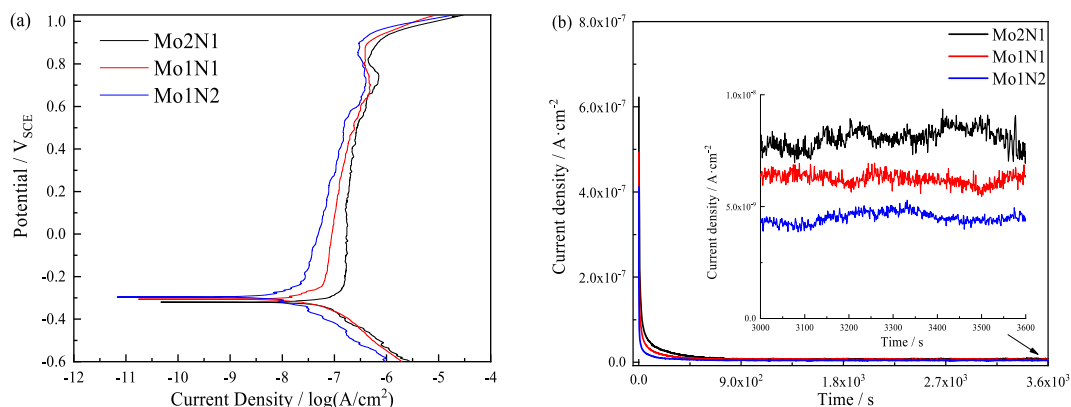| Sample	NH_3 (NH_4^+)/ppm	NO_3/ppm
Mo2N1	1.16	0.02
Mo1N1	1.65	0.02
Mo1N2	2.79	0.01

Fig. 3. Polarization curves in a 3.5% NaCl solution at 50 °C. (a) Dynamic potential polarization curves; (b) Transient current densities.
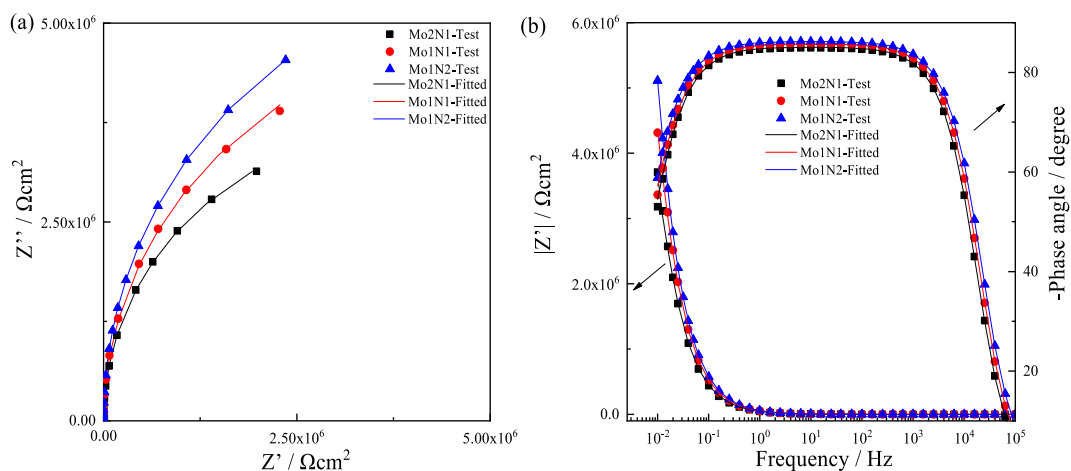

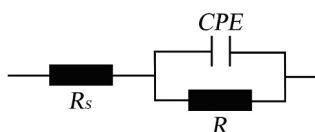**Fig. 4.** Impedance of samples in 3.5 % NaCl liquor at 50 °C. (a) Nyquist; (b) Bode.

Fig. 5. Equivalent circuit diagram.

Table 3
Theoretical impedance values of EIS in 3.5% NaCl solution at 50 °C.

Sample	$R_s/\Omega \cdot cm^2$	$Q/\times10^{-6} \, \Omega^{-1} \, cm^{-2} \cdot s^n$	n	$R/10^6 \, \Omega \, cm^2$	$C/\times10^{-6} \, F \, cm^{-2}$	$\chi^2/\times10^{-4}$
Mo2N1	2.598	3.601	0.9451	7.003	4.344	2.682
Mo1N1	2.667	3.044	0.9544	9.133	3.568	6.212
Mo1N2	2.629	2.664	0.9607	11.01	3.059	7.075

content. According to the potentiostatic data, the passive film is most dense at a Mo content of 3.48 wt percent and an N content of 0.51 wt percent, indicating that variations in N and Mo content affect the density of the passive film. Q, n, and R are derived from the circuit fitting and the capacitance (C) is computed using eq. (2) [41]. According to the calculated C, the oxide thickness of the steady-state passive film d_{OX} could be calculated by eq. (3) [42,43].

$$C = \sqrt[n]{\frac{Q}{R^{n-1}}} \tag{2}$$

$$d_{ox} = \frac{\varepsilon\varepsilon_0 A}{C} \qquad (3)$$

where ε_0 represents the vacuum dielectric constant (8.854×10^{-14} F/cm), ε is the dielectric constant (15.6), and A is the effective area (m^2). Due to the thin film and non-dense outer layer of Fe and Cr hydroxides or hydrides, an accurate estimate of passive film thickness is challenging [44,45]. The decline in capacitance as the N content increases and Mo content falls suggests a thickening of the oxide layer of the steady-state passive film.

3.4. Effect of Mo and N content on the semiconductor properties of the passive film

Passive films possess the characteristics of deeply doped semiconductors. The principal carriers of doped semiconductors with oxygen vacancies or cation interstitials are categorized as n-type, while those with cation vacancies are classified as p-type [46]. The semiconductor capacity using eq. (4) as follows:

$$\frac{1}{C} = \frac{1}{C_{SC}} + \frac{1}{C_H} \qquad (4)$$

Among them, C_{sc} and C_H denote the space charge and Helmholtz capacitance, respectively. When applying a potential perturbation with sufficiently high frequency, C_{sc} becomes very small compared with C_H, so the calculation of interface capacitance can neglect the contribution due to C_H and only consider C_{sc}. Therefore, the potential and space charge capacitance of p-type and n-type semiconductors are eq. (5) and eq. (6) correlated as follows:

$$\frac{1}{C_{cs}^2} = \frac{-2}{\varepsilon\varepsilon_0 e N_A}\left(E - E_{fb} - \frac{kT}{e}\right) \qquad (5)$$

$$\frac{1}{C_{cs}^2} = \frac{2}{\varepsilon\varepsilon_0 e N_D}\left(E - E_{fb} - \frac{kT}{e}\right) \qquad (6)$$

where ε_0 represents the vacuum dielectric constant (8.854×10^{-14} F/cm), ε is the dielectric constant (15.6), and e is the electron charge (1.602×10^{-19} C) [47]. The electron donor density for n-type semiconductors and the vacancy acceptor density for p-type semiconductors are N_D and N_A, respectively, (cm^{-3} units) as derived from the slope of the C^{-2}-E; T is the absolute temperature, k is the Boltzmann constant (1.38×10^{-23} J/K), E represents the applied voltage, and E_{FB} is the flat-band potential, determined by extending to $C^{-2} = 0$.

The M − S plots for the samples presented in Fig. 6 refer to the application of 300 mV (vs. SCE) for 60 min at a constant potential in a 3.5% NaCl solution at 50 °C. Given the commonality of each sample, it can be inferred that the passive films share the same electrical properties. In addition, the C^{-2}-E plot exhibits a positive slope over the potential range 550 mV (vs. SCE) to 0 mV (vs. SCE), suggesting n-type semiconductor properties. In contrast, the slope of C^{-2}-E is negatively sloped in the negative potential range, suggesting p-type semiconductor properties, suggesting that the passive film has dual properties [48].

The calculated values of N_A, N_D, and E_{FB} using the M − S slope are shown in Table 4. With an increase in N and lower Mo contents, N_A and N_D exhibit a declining tendency. The drop in N_A and N_D suggests a reduced passive film defect density and conductivity, which inhibits interfacial reactions [49]. With a rise in N content and a fall in Mo content, E_{FB-n} exhibits an upward tendency. An increase in E_{FB-n} serves to decrease the transfer of electrons from the passive film to the solution, resulting in a lower positive charge of the passive film and a weakening of electrostatic attraction to negatively charged Cl$^-$ because the n type semiconductor is on the outer side of the
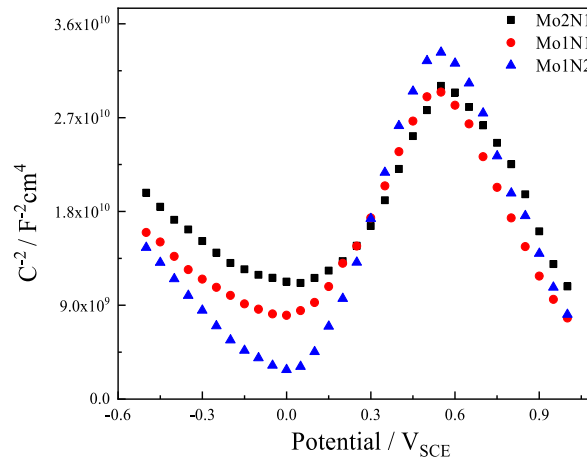

Fig. 6. M–S in 3.5 % NaCl solution at 50 °C.

Table 4

N_A, N_D, and E_{FB} in 3.5 % NaCl solution at 50 °C.

Sample	Acceptor density, $N_A \times 10^{-20}/cm^{-3}$	E_{FB-p} /V_{SCE}	Donor density, $N_D \times 10^{-20}/cm^{-3}$	E_{FB-n} /V_{SCE}
Mo2N1	4.011784	0.36774	1.813179	−0.04110
Mo1N1	3.898148	0.18804	1.620519	−0.01834
Mo1N2	3.138498	−0.00120	1.151590	0.07874

passive film, which is in touch with the solution [23].

3.5. Influence of Mo and N on passive film composition and thickness

Fig. 7(a) and (b-d) illustrate the non-soaked Mo1N2 and soaked samples after soaking in 3.5% NaCl solution at 50 °C for 24 h. The average passive film thicknesses measured at five locations are given in Table 5. The values in Fig. 7 and Table 5 reveal that the passive films of the non-soaked samples are thinner than the soaked ones and that the passive films of Mo1N2 are thicker. This is likely the cause of the lower potentiostatic current, higher resistance, and lower N_A and N_D of Mo1N2.

The depth distribution of component concentrations in the passive films of the three samples is shown in Fig. 8(a–c) for a 3.5 % NaCl solution at 50 °C. It is evident that the external contamination layer is associated with the passive layer. The contamination layer is composed of complex organic molecules with a significant C concentration [50] that is reduced as the sputtering process proceeds. The rate of Cr to O in Mo2N1, Mo1N1, and Mo1N2 increases over the same sputtering time in that order, indicating that the passive films of Mo2N1, Mo1N1, and Mo1N2 thicken in that order, which is consistent with the thickness of the passive films given in Fig. 7 and Table 5. The Fe, Ni, and Cr content tend to increase with sputtering time to match the matrix content.

The photoelectron spectra of Cr2p$_{3/2}$, Fe2p$_{3/2}$, Mo3d, and N1s were fitted to the binding energies given in Table 6 [51–56], and the fitted data of the photoelectron spectra of Cr2p$_{3/2}$, Fe2p$_{3/2}$, Mo3d, and N1s are shown in Figs. 9 and 10.

Figs. 9 and 10 demonstrate that CrO_4^{2-}, $Cr(OH)_3$, Cr_2O_3, and Cr_{met} make up the majority of the Cr2p$_{3/2}$ spectrum. The Mo3d spectrum is dominated by MoO_4^{2-}, MoO_2, and Mo_{met}, whereas N1s are dominated by NH_4^+ and N_{atom}. In addition, the Fe2p$_{3/2}$ spectrum is dominated by Fe_2O_3, FeO, Fe_3O_4, Femet, and FeOOH. According to the Pourbaix diagram in Fig. 11, under neutral conditions, Fe, Cr, Mo, and N dissolve to produce stable compounds such as CrO_4^{2-}, Fe_2O_3, MoO_4^{2-}, and N at a potential of 300 mV (vs. SCE). The Pourbaix diagram was created using thermodynamic data for known bulk compounds [51], although thermodynamics was unsuccessful in predicting the compounds in the passive film, the overall trend was consistent with thermodynamic predictions. More species were detected in the XPS analysis than are present in the Pourbaix diagram, further indicating that the formation of passive films is a dynamic equilibrium between the generation and dissolution processes.

Fig. 9(a) and 10(a) show that at the beginning of sputtering, the Cr2p$_{3/2}$ composition follows the order: $Cr(OH)_3$, CrO_4^{2-}, Cr_2O_3, Cr_{met}. As the duration of sputtering increases, $Cr(OH)_3$ and CrO_4^{2-} are reduced, Cr_2O_3 increases and, ultimately, only Cr_{met} is present. As illustrated in Fig. 9(b) and 10(b), at the beginning of sputtering the Fe2p$_{3/2}$ compound content is in the order: Fe_2O_3, Fe_3O_4, FeOOH, FeO, Femet. With an increase in sputtering time, FeO and FeOOH decrease rapidly, and Fe_3O_4 and Fe_2O_3 increase slowly and then decrease gradually. Fe_3O_4 is a compound oxide consisting of Fe^{2+} and Fe^{3+}, that might be represented by $FeO \cdot Fe_2O_3$ [57]. Fig. 9(c) and 10(c) indicate that at the beginning of sputtering, the Mo3d compounds are MoO_4^{2-}, MoO_2, and Mo_{met}. With increasing sputtering time, MoO_4^{2-} shows a fast decrease in the surface layer, whereas MoO_2 exhibits a slight increase. Fig. 9(d) and 10(d) illustrate how the contribution to N1s due to NH_4^+ content is higher than the N_{atom} content at the start of sputtering, with N_{atom} rising and NH_4^+ falling as sputtering time increases.

With increasing sputtering time, the rates of Cr_2O_3 to $Cr(OH)_3+CrO_4^{2-}$ (Fig. 10(a)), Fe_{OX}^{3+}(Fe^{3+} oxide) to Fe_{OX}^{2+} (Fe^{2+} oxide) (Fig. 10(b)), Mo ions/Mo (Fig. 10(c)) all increase, and NH_4^+ disappears after 30s. This indicates that Cr_2O_3 and Fe_{OX}^{3+} predominate in the inner layer of the passive film, and CrO_4^{2-}, $Cr(OH)_3$, Fe_{OX}^{2+}, MoO_2, MoO_4^{2-} and NH_4^+ are found in the outer layer. The results suggest that following exposure to the solution, the test steel formed Cr, Fe, and Mo ions on the surface, which led to the creation and expansion of
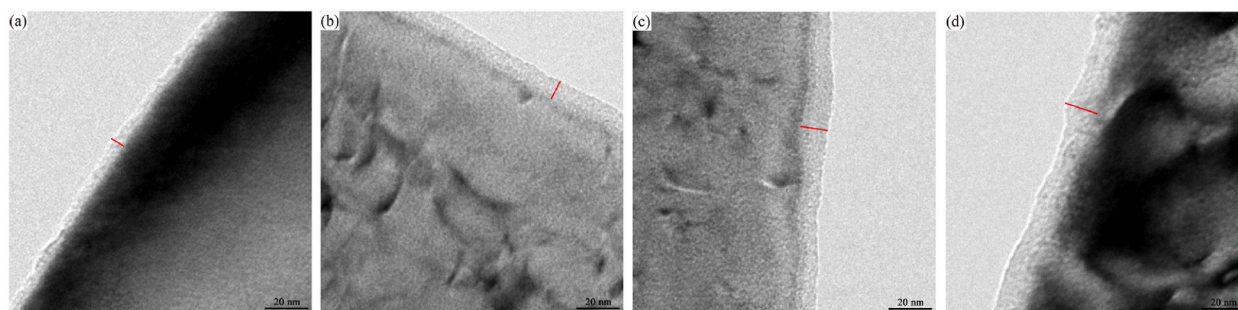

Fig. 7. TEM images of passive films with and without immersion in a 3.5% NaCl solution at 50 °C for 24 h (a) Non-soaked sample of Mo1N2; (b) Mo2N1; (c) Mo1N1; (d) Mo1N2.

Table 5
Thickness of passive films after 24 h immersion in a 3.5% NaCl solution at 50 °C.

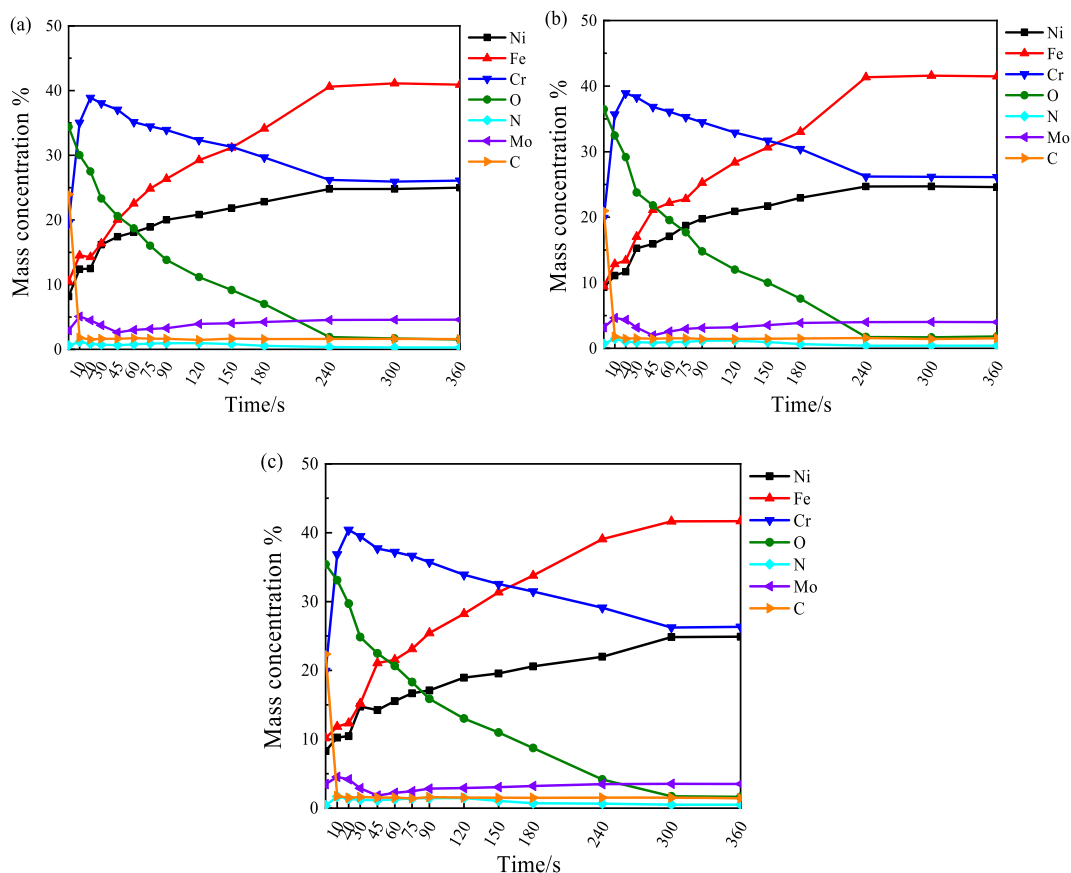| Sample	average value/nm
Non-soaked Mo1N2	6.53
Mo2N1	10.01
Mo1N1	11.02
Mo1N2	13.52

Fig. 8. Depth distribution of individual sample component contents in a 3.5% NaCl solution at 50 °C (a) Mo2N1; (b) Mo1N1; (c) Mo1N2.

Cr due to its relatively high negative Gibbs free energy in comparison to other materials [58]. As $Cr(OH)_3$ possesses a lower standard free energy [59], it is first generated in eq. (7) and converted in eq. (8) and eq. (9) to yield CrO_4^{2-} and Cr_2O_3.

$$4\,Cr^{3+} + 3\,O_2 + 6\,H_2O + 12\,e^- \rightarrow 4\,Cr(OH)_3 \tag{7}$$

$$Cr(OH)_3 + 5\,OH^- \rightarrow CrO_4^{2-} + 4\,H_2O + 3\,e^- \tag{8}$$

$$4\,Cr(OH)_3 + 4\,Cr + 3\,O_2 \rightarrow 4\,Cr_2O_3 + 6H_2O \tag{9}$$

As the N content increases and the Mo content decreases, the rate of Cr_2O_3 to $Cr(OH)_3 + CrO_4^{2-}$ (Fig. 10(a)), Fe_{OX}^{3+}(Fe^{3+} oxide) to Fe_{OX}^{2+} (Fe^{2+} oxide) (Fig. 10(b)), Mo ions/Mo (Fig. 10(c)) and NH_4^+ (Fig. 10(d)) increase. Fig. 10(c) reveals that the MoO_4^{2-} content grows as the N content grows. This is because N is present in austenitic stainless steels as interstitial atoms, and when these atoms come into contact with aqueous solutions, they dissolve to produce NH_4^+ (eq. (10)), effectively raising the local pH, which may cause the electrode response to shift to a higher pH and favor MoO_4^{2-}[60]. MoO_4^{2-} converts the passive film to a bipolarized film with an anion-selective inner layer and a cation-selective outer layer. This bipolarized film prevents surface Cl^- from penetrating the passive film and also causes deprotonation of the inner region of the bipolar film interface due to the applied anodic potential (eq. (11)), which causes proton loss into the solution via the cation-selective outer layer. The O^{2-} ions produced by OH^- deprotonation prefer to migrate towards the metal surface, promoting the formation of denser Cr_2O_3. Moreover, MoO_2 increases the homogeneity of the passive film as

Table 6
Binding energy of Cr, Fe, Mo, and N associated with different compounds.

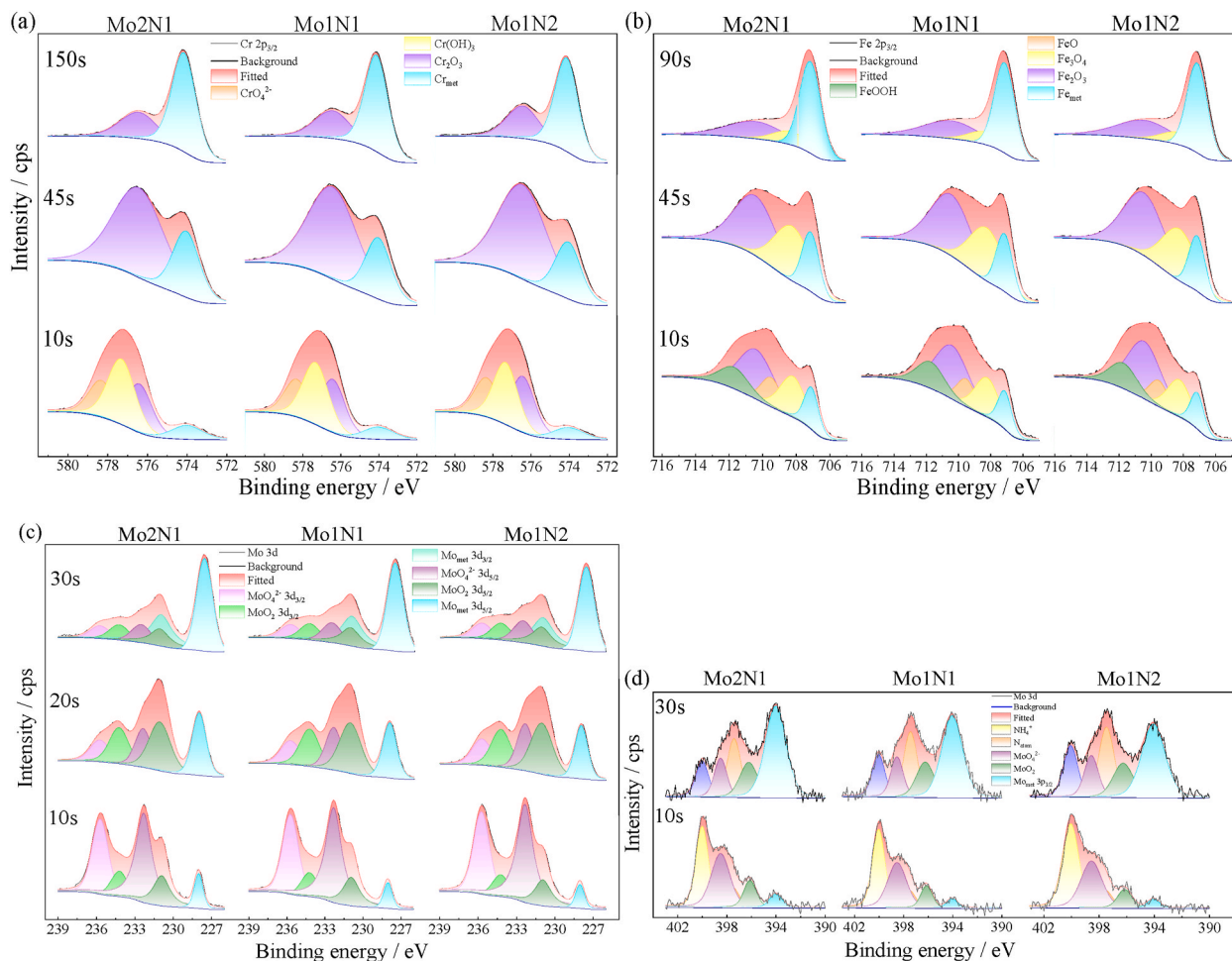| Element	Valence state	Binding energy/eV
Cr	Cr_{met}	574.0 ± 0.1
	CrO_4^{2-}	578.3 ± 0.1
	$Cr(OH)_3$	577.3 ± 0.1
	Cr_2O_3	576.4 ± 0.1
Fe	Fe_{met}	707.1 ± 0.1
	FeOOH	711.7 ± 0.1
	Fe_2O_3	710.4 ± 0.1
	FeO	709.5 ± 0.1
	Fe_3O_4	708.2 ± 0.1
Mo	$(Mo_{met}):Mo3d_{5/2}$、$Mo3d_{3/2}$	228.0 ± 0.1、230.9 ± 0.1
	$MoO_2:Mo3d_{5/2}$、$Mo3d_{3/2}$	231.0 ± 0.1、234.2 ± 0.1
	$MoO_4^{2-}:Mo3d_{5/2}$、$Mo3d_{3/2}$	232.3 ± 0.1、235.7 ± 0.1
N	N_{atom}	397.5 ± 0.1
	NH_4^+	400.0 ± 0.1
	$MoO_4^{2-}3p_{3/2}$	398.5 ± 0.1
	$MoO_23p_{3/2}$	396.1 ± 0.1
	Mo_{met}	394.0 ± 0.1

Fig. 9. Cr2p3/2, Fe2p3/2, Mo3d, N1s photoelectron spectra at different times (a) $Cr2p_{3/2}$; (b) $Fe2p_{3/2}$; (c) Mo3d; (d) N1s.

the anion-selective layer prevents the migration of the inner cations, and a positive ionic space charge is formed [60,61]. An increase in Cr_2O_3 density provides better protection [62]. This accounts for the fact that the resistance and n values of the passive film in the preceding section exhibit an upward trend with increasing N content and falling Mo content, while the N_D and N_A of the passivated film
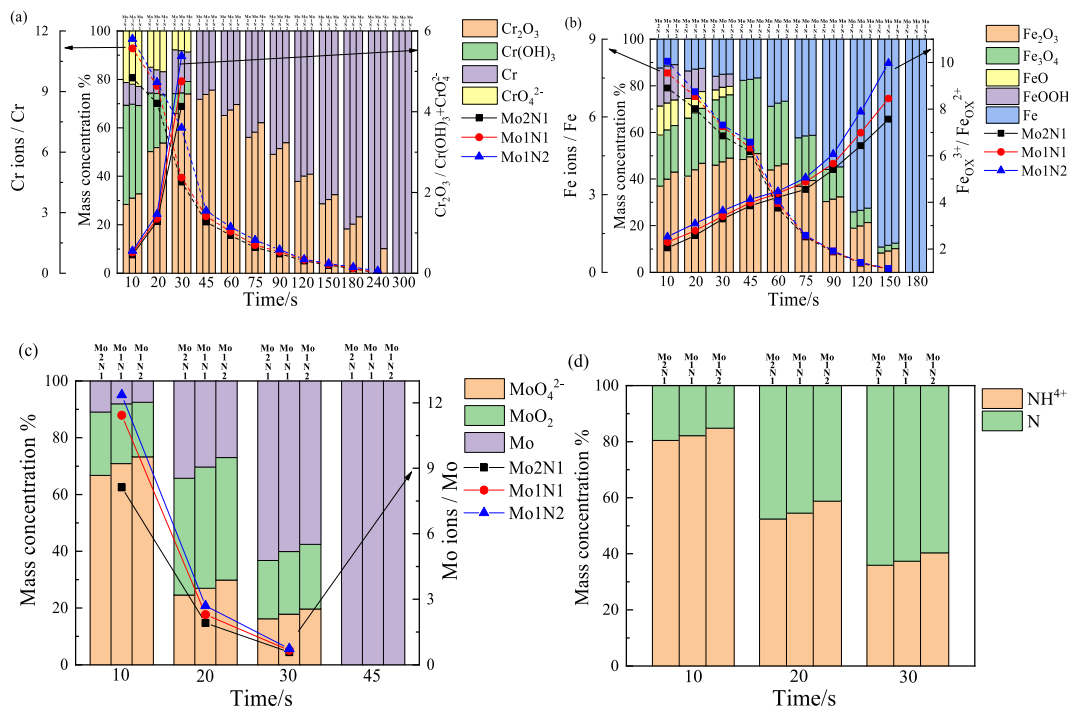
Fig. 10. Mass concentration and ratio (a) Cr, Cr ions/Cr and $Cr_2O_3/Cr(OH)_3+CrO_4^{2-}$; (b) Fe, Fe ions/Fe and $Fe_{OX}^{3+}/Fe_{OX}^{2+}$; (c) Mo, Mo ions/Mo; (d) N.
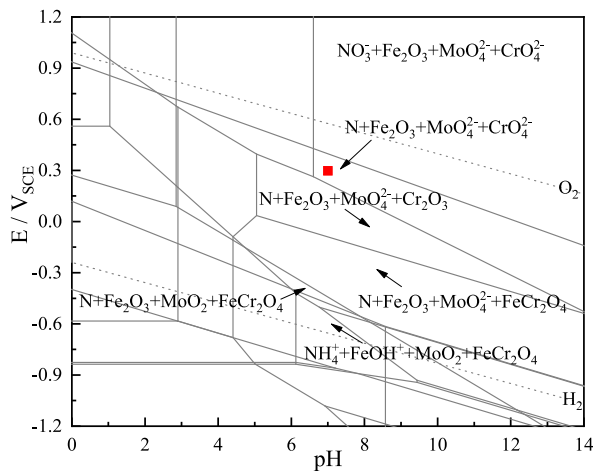

Fig. 11. Pourbaix diagram of the Fe–Cr–Mo–N system of alloys in water at 50 °C.

exhibit the opposite tendency with rising N content and falling Mo content.

$$N + 4\,H^+ + 3\,e^- \rightarrow NH_4^+ \tag{10}$$

$$2\,Cr(OH)_3 \rightarrow Cr_2O_3 + 2\,O^{2-} + 4\,H^+ \tag{11}$$

3.6. Impact of Mo and N doping on the resistance of passive films to NaCl adsorption

To study the synergistic influence of Mo and N on the passivation film, six models were constructed based on a Fe_2O_3: Fe_2O_3 model: $1Mo$–Fe_2O_3 surface 1 Fe atom replaced by a Mo atom [63]; $1N$–Fe_2O_3 surface 1 O atom replaced by a N atom; $1Mo1N$–Fe_2O_3 surface 1 Fe atom replaced by a Mo atom and 1 O atom replaced by a N atom, respectively; $2Mo1N$–Fe_2O_3 surface 2 Fe atoms replaced by 2 Mo atoms and 1 O atom replaced by a N atom; $1Mo2N$–Fe_2O_3 surface 1 Fe atom replaced by Mo atom and 2 O atom replaced by a N atom, respectively. The most stable structure for the six models created by the computations was found through a variety of structural

optimizations due to the high number of structures following surface doping, as shown in Fig. 12(a–f).

Calculations of NaCl adsorption were performed at 3.5 Å above the four atoms on the surface after constructing the model. The equation for adsorption energy (E_{ads}) is expressed in Equation (12):

$$E_{ads} = E_{NaCl+Film} - E_{NaCl} - E_{Film} \qquad (12)$$

Where $E_{NaCl\ +\ Film}$ represents the surface energy of (0001) after adsorption of 1 NaCl, E_{Film} is the surface energy of (0001) without NaCl adsorption, and E_{NaCl} is the energy of a single NaCl. The charge transfer (ΔQ) produced by Cl after the adsorption of 1 NaCl can be described as Equation (13):

$$\Delta Q = Q_{NaCl} - Q_{ads} \qquad (13)$$

Where Q_{ads} denotes the Cl charge in the adsorbed NaCl molecule, and Q_{NaCl} denotes the Cl charge in an isolated NaCl molecule (7.84794 e). Positive values represent electron loss and negative values represent electron gain. The equation of the work function W may be expressed as Equation (14):

$$W = E_{vacuum} - E_F \qquad (14)$$

Where E_{vacuum} denotes the vacuum energy level and E_F is the Fermi energy. A lower W represents a greater vulnerability to corrosion [63–65].

Following completion of the adsorption computation, the surface relaxes as a result of a change in the environment in which the atoms on the surface are placed, with displacements occurring along various directions. The a-coordinate of the initial position of the adsorbed atoms is defined as d_1, and following the calculation, the coordinates of the atoms change to d_2. It was found that after NaCl adsorption, the relaxation is mainly in the a-direction, with smaller displacements in other directions. The magnitude of the relaxation in the a-direction is measured using $\Delta d = d_2 - d_1$; $\Delta d > 0$ indicates increasing movement in the a-direction, away from the surface, and $\Delta d < 0$ indicates relaxation in the direction of the bulk phase [63].

The E_{ads}, adsorption distances, bond lengths, W, and Δd at different adsorption sites for the different adsorption models are given in Table 7. The E_{ads} values are all negative, indicating exothermic reactions. The W associated with 1Mo raises the W of pure Fe_2O_3 by 0.05747 eV [63] and the contribution of 1 N increases the W of pure Fe_2O_3 by 0.08386 eV. Moreover, 1Mo1N increases the W of pure Fe_2O_3 by 0.23928 eV, more than the sum of the respective increases due to 1Mo and 1 N. In addition, 2Mo1N raises the W of pure Fe_2O_3 by 0.31489 eV, more than the sum of the respective increases due to 1Mo1N and 1Mo. As a final observation, 1Mo2N increases the W of pure Fe_2O_3 by 0.47424 eV, more than the sum of the respective increases due to 1Mo1N and 1 N. These effects suggest a synergistic relationship between Mo and N where the corrosion resistance of the passive film is strengthened with increasing Mo and N content, with N playing a more prominent role.

As can be seen for 1Mo1N, 2Mo1N, and 1Mo2N in Table 7, the co-existence of Mo and N led to a more pronounced rise in adsorption energy, with the adsorption energy of Mo in 1Mo1N increasing from -73.19845 kJ•mol^{-1} to -55.53591 kJ•mol^{-1} in the 1Mo model. The adsorption energy of Fe, the next closest neighbor to N in 1Mo1N, is raised to -48.22041 kJ•mol^{-1} compared with -52.21393 kJ•mol^{-1}. In the case of the 1Mo2N model, the adsorption energies of all three adsorption sites are significantly higher than those of 2Mo1N, indicating that N plays a greater role and the increase in adsorption energy is not merely the result of replacing atoms alone but the result of synergistic effect.

The bond lengths, displacements, and ΔQ after adsorption for the six models show that the bond lengths are positively correlated with the adsorption energy, and Δd and ΔQ are negatively correlated with the adsorption energy. The longer the bond length, the smaller ΔQ and Δd, and the smaller the interatomic forces, indicating that NaCl destabilizes the structure of the passive film to a lesser degree [66]. ΔQ is slightly larger for the Mo atom as the adsorption site when compared with Fe as the adsorption site, which may be caused by the higher number of electrons outside the nucleus in the case of Mo.

The differential charge density of NaCl adsorbed at different locations on different surfaces is shown in Fig. 13. The yellow color indicates greater charge density, whereas cyan indicates lower charge density. As shown in Fig. 13(a)–(q), it is evident that Cl shares electrons with the surface, suggesting the formation of chemical bond. It is also evident from Fig. 13(d)–(q) that there is greater charge transfer from the doped N atom to the nearby metal atom when NaCl is adsorbed on a Fe or Mo atom. Moreover, the two-dimensional cross-sectional picture of the differential charge density (top right tiny panel of Fig. 13) demonstrates how few electrons Na are acquired and lost upon adsorption.

The limitations of this study are the accuracy of the test apparatus, financial constraints, the solubility of N in steel, and the experimental difficulty in verifying the results of the simulations. From the available tests and simulations, it can be seen that in super austenitic stainless steels with a Cr content of 26 percent, a Mo content of 3.5–4.5 percent, and an N content of 0.3–0.5 percent. When fixing the PREN increasing the N content of super austenitic stainless steel and reducing the Mo content can improve corrosion resistance, while reducing hot crack sensitivity with lower costs and an improved yield.

4. Conclusions

1. The passive film of super austenitic stainless steel in a 3.5% NaCl solution at 50 °C is primarily bilayered, with Cr_2O_3 and Fe_{OX}^{3+} as the inner layer and CrO_4^{2-}, $Cr(OH)_3$, Fe_{OX}^{2+}, MoO_2, and MoO_4^{2-} as the outer layer. The Cr_2O_3 and Fe_{OX} content increases and becomes more continuous at the same thickness as the test steel N content is increased from 0.29 wt% to 0.51 wt% and the Mo content falls
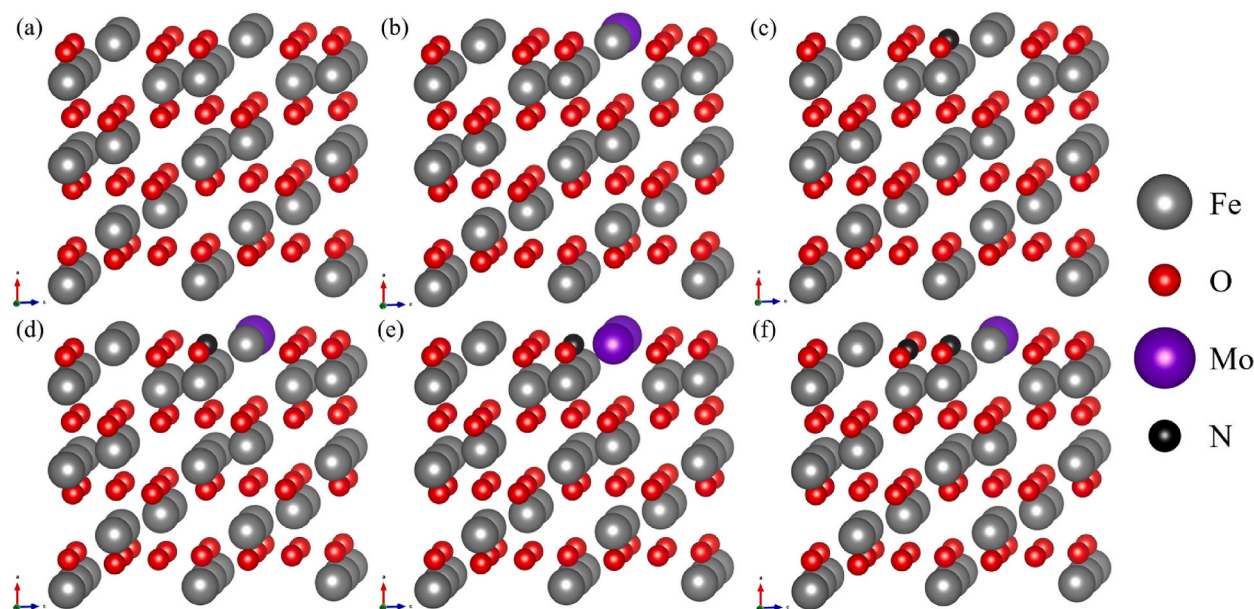
Fig. 12. Models constructed. (a) Fe$_2$O$_3$; (b) 1Mo; (c) 1 N; (d) 1Mo1N; (e) 2Mo1N; (f) 1Mo2N.

Table 7
E$_{ads}$, bond lengths, ΔQ, Δd, and W values for the different adsorption models.

Models	adsorption site	E$_{ads}$/kJ mol^{-1}	bond distance/Å	W/eV	Δd/Å	ΔQ/e
Fe$_2$O$_3$	Fe	−82.79196	2.28692	4.19675	0.01537	0.16721
1Mo	Mo	−73.19845	2.40037	4.25422	0.00749	0.17546
	Fe	−62.84754	2.30214		0.01394	0.15267
1 N	Fe1	−45.46480	2.34582	4.28061	0.01258	0.13981
	Fe2	−61.12625	2.30949		0.01362	0.14973
	Fe3	−65.48255	2.29333		0.01416	0.15439
1Mo1N	Mo	−55.53591	2.41013	4.43603	0.00701	0.17292
	Fe1	−48.22041	2.33245		0.01262	0.14003
	Fe2	−52.21393	2.32161		0.01289	0.14212
2Mo1N	Mo1	−44.04068	2.41298	4.51164	0.00663	0.17091
	Fe1	−38.10686	2.39053		0.01186	0.09822
	Mo2	−43.18872	2.41659		0.00652	0.17062
	Fe2	−42.24799	2.37092		0.01219	0.12072
1Mo2N	Mo	−39.93139	2.42317	4.67099	0.00644	0.16958
	Fe1	−32.28785	2.40654		0.01121	0.09076
	Fe2	−43.04206	2.36511		0.01227	0.12613
	Fe3	−36.75310	2.39665		0.01166	0.09525

from 4.52 wt% to 3.48 wt%, producing a thicker and more uniform passive film. This leads to lower N$_A$ and N$_D$, higher resistance and E$_{FB-n}$, and a consequent lower space charge conductivity. The passive film is less likely to react with external Cl$^-$, which in turn leads to a reduction in passive current density, critical current density, and constant potential current density, resulting in increased corrosion resistance.

2. During immersion corrosion, the passive film is more homogeneous and contains more Cr$_2$O$_3$, which results in fewer active sites to initiate pitting corrosion, a smaller number of pitting pits, and a tendency for the NH$_3$(NH^{4+}) content in the pitting pits to increase, raising the local pH of the pitting pits and slowing the rate of pitting expansion. Less active pitting sites in the passive film, the occurrence of delayed pitting corrosion sprouting, and NH$_3$(NH^{4+}) mitigation of local acidity all work together to reduce the maximum area and depth of pitting.

3. The enhancement in adsorption energy and W caused by the simultaneous doping of Mo and N is significantly greater than the enhancement in adsorption energy and W caused by doping of Mo and N alone, indicating that the enhancement in W and adsorption energy is not simply a single effect following atom replacement, but the result of a complex synergism.

Data availability statement

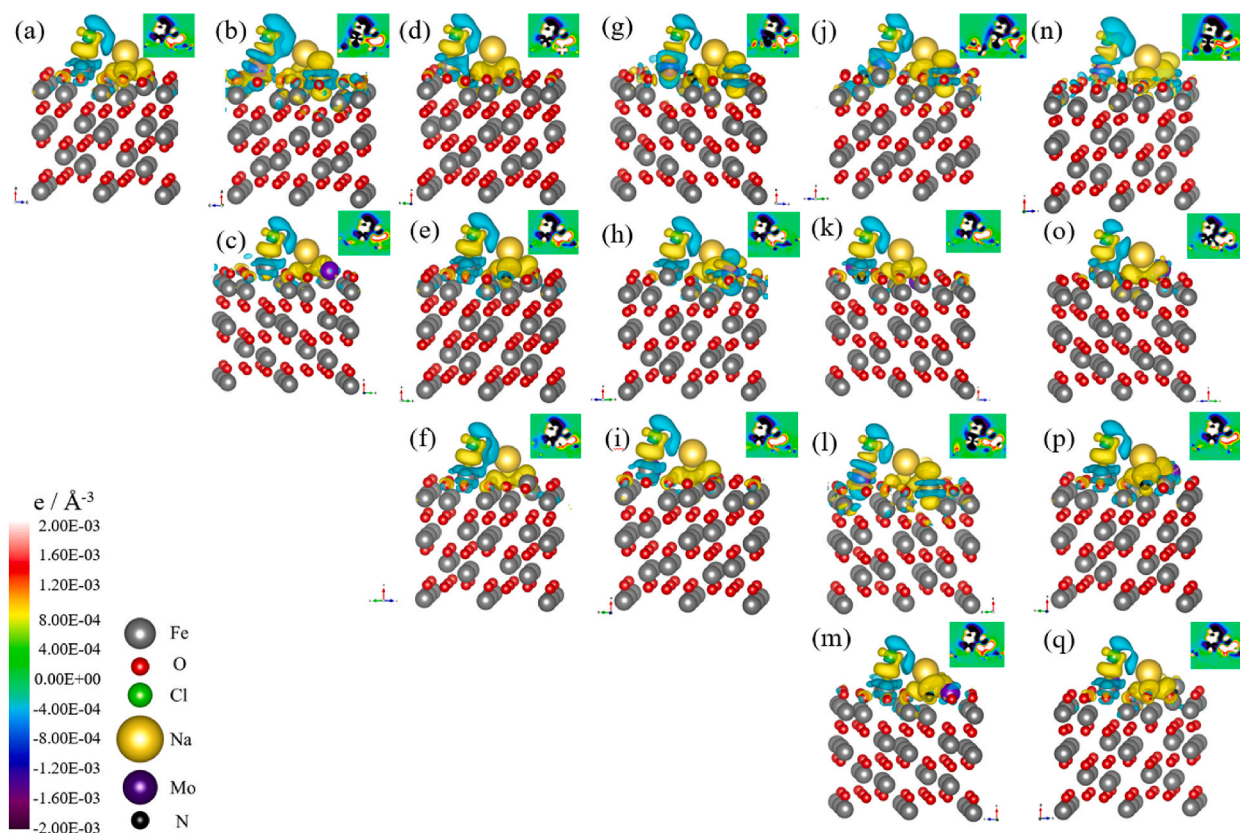Data included in article and referenced in the article.

Fig. 13. Differential charge density of NaCl molecules adsorbed on different surfaces at different positions. (a) Fe_2O_3; (b) 1Mo–Mo; (c) 1Mo–Fe; (d) 1N–Fe1; (e) 1N–Fe2; (f) 1N–Fe3; (g)1Mo1N–Mo; (h) 1Mo1N–Fe1; (i) 1Mo1N–Fe2; (j) 2Mo1N–Mo1; (k) 2Mo1N–Fe1; (l) 2Mo1N–Mo2; (m) 2Mo1N–Fe2; (n) 1Mo2N–Mo; (o) 1Mo2N–Fe1; (p) 1Mo2N–Fe2; (q) 1Mo2N–Fe3.

CRediT authorship contribution statement

Bingbing Li: Writing – review & editing. **Yuping Lang:** Methodology. **Haitao Chen:** Data curation. **Hanqiu Feng:** Investigation. **Huapeng Qu:** Methodology. **Xu Sun:** Methodology. **Zhiling Tian:** Supervision.

Declaration of competing interest

The authors declare that they have no known competing financial interests or personal relationships that could have appeared to influence the work reported in this paper.

References

[1] J. Anburaj, S.S.M. Nazirudeen, R. Narayanan, et al., Ageing of forged super austenitic stainless steel :precipitate phases and mechanical properties, J. Mater. Sci. Eng. 535 (2012) 99–107, https://doi.org/10.1016/j.msea.2011.12.048.
[2] C. Muller, L.S. Chumbley, Fracture toughness of heat-treated superaustenitic stainless steels, J. Mater. Eng. Perform. 19 (2010) 714–720, https://doi.org/10.1007/s11665-009-9533-4.
[3] K.H. Lo, C.H. Shek, J.K.L. Lai, Recent developments in stainless steels, Mater. Sci. Eng. R. 65 (2009) 39–104, https://doi.org/10.1016/j.mser.2009.03.001.
[4] H.H. Strehblow, V. Maurice, P. Marcus, Passivity of Metals, Corros. Technol. CRC Press, 2011.

[5] A.R. Brooks, C.R. Clayton, K. Doss, Y.C. Lu, On the role of Cr in the passivity of stainless steel, J. Electrochem. Soc. 133 (1986) 2459–2464, https://doi.org/10.1149/1.2108450.

[6] P. Marcus, M.E. Bussell, XPS study of the passive films formed on nitrogen-implanted austenitic stainless steels, Appl. Surf. Sci. 59 (1992) 7–21, https://doi.org/10.1016/0169-4332(92)90163-R.

[7] G. Mori, D. Bauernfeind, Pitting and crevice corrosion of superaustenitic stainless steels, Mater. Corros. 55 (2004) 164–173, https://doi.org/10.1002/MACO.200303746.

[8] S. Nagarajan, N. Rajendran, Crevice corrosion behaviour of superaustenitic stainless steels: dynamic electrochemical impedance spectroscopy and atomic force microscopy studies, Corrosion Sci. 51 (2009) 217–224, https://doi.org/10.1016/j.corsci.2008.11.008.

[9] C.O.A. Olsson, The influence of nitrogen and molybdenum on passive films formed on the austenoferritic stainless steel 2205 studied by AES and XPS, Corrosion Sci. 37 (1995) 467–479, https://doi.org/10.1016/0010-938X(94)00148-Y.

[10] Y.C. Lu, M.B. Ives, C.R. Clayton, Synergism of alloying elements and pitting corrosion resistance of stainless steels, Corrosion Sci. 35 (1993) 89–96, https://doi.org/10.1016/0010-938X(93)90137-6.

[11] C.R. Clayton, Y.C. Lu, A Bipolar Model of the passivity of stainless steel: the role of Mo addition, J. Electrochem. Soc. 133 (1986) 2465–2473, https://doi.org/10.1149/1.2108451.

[12] M.B. Ives, Y.C. Lu, J.L. Luo, Cathodic reactions involved in metallic corrosion in chlorinated saline environments, Corrosion Sci. 32 (1991) 91–102, https://doi.org/10.1016/0010-938X(91)90065-W.

[13] G.S. Frankel, Pitting corrosion of metals: a review of the critical factors, J. Electrochem. Soc. 145 (1998) 2186–2198, https://doi.org/10.1149/1.1838615.

[14] H. Baba, T. Kodama, Y. Katada, Role of nitrogen on the corrosion behavior of austenitic stainless steels, Corrosion Sci. 44 (2002) 2393–2407, https://doi.org/10.1016/S0010-938X(02)00040-9.

[15] D.P. Le, W.S. Ji, J.G. Kim, et al., Effect of antimony on the corrosion behavior of low-alloy steel for flue gas desulfurization system, Corrosion Sci. 50 (2008) 1195–1204, https://doi.org/10.1016/j.corsci.2007.11.027.

[16] M. Liu, X. Chen, X. Li X, et al., Effect of Cr on the passive film formation mechanism of steel rebar in saturated calcium hydroxide solution, Appl. Surf. Sci. 389 (2016) 1182–1191, https://doi.org/10.1016/J.APSUSC.2016.08.074.

[17] G. Kresse, J. Furthmüller, Efficient iterative schemes for ab initio total-energy calculations using a plane-wave basis set, Phys. Rev. B 54 (1996) 11169–11186, https://doi.org/10.1103/PhysRevB.54.11169.

[18] J.P. Perdew, K. Burke, M. Ernzerh, Generalized gradient approximation made simple, Phys. Rev. Lett. 77 (1996) 3865–3868, https://doi.org/10.1103/PhysRevLett.77.3865.

[19] X. Li, L. Chen, H. Liu, 2 Mi, C. Shi, L. Qiao, Atom doping in a-Fe$_2$O$_3$ thin films to prevent hydrogen permeation, Int. J. Hydrogen Energy 44 (2019) 3221–3229, https://doi.org/10.1016/j.ijhydene.2018.11.181.

[20] Q. Pang, H. Dormohammadi, O. Burkan Isgor, L. Arnadóttir, The effect of surface vacancies on the interactions of CI with the a- Fe$_2$O$_3$ (0001) surface and the role of Cl in depassivation, Corrosion Sci. 154 (2019) 61–69, https://doi.org/10.1016/j.corsci.2019.03.052.

[21] B.B. Li, Y.P. Lang, H.T. Chen, et al., Copper content effects on passive film of modified 00Cr20Ni18Mo6CuN super austenitic stainless steels in acidic environment, Heliyon 9 (2023) e13652, https://doi.org/10.1016/j.heliyon.2023.e13652.

[22] Z.H. Mi, L. Chen, C. Shi, Y. Ma, D. Wang, X. Li, H. Liu, L. Qiao, The effects of strain and vacancy defects on the electronic structure of Cr$_2$O$_3$, Comput. Mater. Sci. 144 (2018) 64–69, https://doi.org/10.1016/J.COMMATSCI.2017.12.012.

[23] D. Chen, C. Dong, Y. Ma, et al., Revealing the inner rules of PREN from electronic aspect by first-principles calculations, Corrosion Sci. 189 (2021) 109561, https://doi.org/10.1016/j.corsci.2021.109561.

[24] E. Sanville, S.D. Kenny, R. Smith, et al., Improved grid-based algorithm for Bader charge allocation, J. Comput. Chem. 28 (2007) 899–908, https://doi.org/10.1002/jcc.20575.

[25] M. Yu, D.R. Trinkle, Accurate and efficient algorithm for Bader charge integration, J. Chem. Phys. 134 (2011) 064111, https://doi.org/10.1063/1.3553716.

[26] G. Makov, M.C. Payne, Periodic boundary conditions in ab initio calculations, Phys. Rev. B Condens. Matter 51 (1995) 4014–4022, https://doi.org/10.1103/PhysRevB.51.4014.

[27] P. Saravanan, V.S. Raja, S. Mukherjee, Effect of alloyed molybdenum on corrosion behavior of plasma immersion nitrogen ion implanted austenitic stainless steel, Corrosion Sci. 74 (2013) 106–115, https://doi.org/10.1016/j.corsci.2013.04.030.

[28] J H Dong Wei, J. Tong, et al., The electrochemical characteristics of Cr30Mo2 ultra pure ferritic stainless steel in NaCl solutions at different temperatures, Int. J. Electrochem. Sci. 8 (1) (2013) 887–902, https://doi.org/10.1016/S1452-3981(23)14065-X.

[29] H. Heon-Young, L. Tae-Ho, B. Jee-Hwan, et al., Molybdenum effects on pitting corrosion resistance of FeCrMnMoNC austenitic stainless steels, J].Metals 8 (8) (2018) 653, https://doi.org/10.3390/met8080653.

[30] S. Nagarajan, M. Karthega, N. Rajendran, Pitting corrosion studies of super austenitic stainless steels in natural sea water using dynamic electrochemical impedance spectroscopy, J. Appl. Electrochem. 37 (2) (2007) 195–201, https://doi.org/10.1007/s10800-006-9231-y.

[31] R.M. Fernández-Domene, E. Blasco-Tamarit, D.M. García-García, et al., Passive and transpassive behaviour of Alloy 31 in a heavy brine LiBr solution, Electrochim. Acta 95 (2013) 1–11, https://doi.org/10.1016/j.electacta.2013.02.024.

[32] Sérgio Luiz de Assis, S. Wolynec, I. Costa, Corrosion characterization of titanium alloys by electrochemical techniques, Electrochim. Acta 51 (2006) 1815–1819, https://doi.org/10.1016/j.electacta.2005.02.121.

[33] A. Igual Muñoz, J. García Antón, J.L. Guiñón, et al., Inhibition effect of chromate on the passivation and pitting corrosion of a duplex stainless steel in LiBr solutions using electrochemical techniques, Corrosion Sci. 49 (2007) 3200–3225, https://doi.org/10.1016/j.corsci.2007.03.002.

[34] J. Pan, D. Thierry, C. Leygraf, Electrochemical impedance spectroscopy study of the passive oxide film on titanium for implant application, Electrochim. Acta 41 (1996) 1143–1153, https://doi.org/10.1016/0013-4686(95)00465-3.

[35] Valero Vidal, A. Igual Muñoz, Study of the adsorption process of bovine serum albumin on passivated surfaces of CoCrMo biomedical alloy, Electrochim. Acta 55 (2010) 8445–8452, https://doi.org/10.1016/j.electacta.2010.07.028.

[36] F.B. Growcock, R.J. Jasinski, Time-Resolved impedance spectroscopy of mild steel in concentrated hydrochloric acid, J. Electrochem. Soc. 136 (1989) 2310–2314, https://doi.org/10.1149/1.2097847.

[37] W.D. Robertson, Molybdate and tungstate as corrosion inhibitors and the mechanism of inhibition, J. Electrochem. Soc. 98 (1951) 94–100, https://doi.org/10.1149/1.2778118.

[38] W. Fredriksson, D. Petrini, K. Edström, et al., Corrosion resistances and passivation of powder metallurgical and conventionally cast 316L and 2205 stainless steels, Corrosion Sci. 67 (2013) 268–280, https://doi.org/10.1016/j.corsci.2012.10.021.

[39] R.H. Jung, H. Tsuchiya, S. Fujimoto, XPS characterization of passive films formed on Type 304 stainless steel in humid atmosphere, Corrosion Sci. 58 (2012) 62–68, https://doi.org/10.1016/j.corsci.2012.01.006.

[40] B.B. Li, H.P. Qu, Y.P. Lang, et al., Copper alloying content effect on pitting resistance of modified 00Cr20Ni18Mo6CuN super austenitic stainless steels, Corrosion Sci. 173 (2020) 108791, https://doi.org/10.1016/j.corsci.2020.108791.

[41] L. Wang, C. Dong, J. Yao, et al., The effect of η-Ni3Ti precipitates and reversed austenite on the passive film stability of nickel-rich Custom 465 steel, Corrosion Sci. 154 (2019) 178–190, https://doi.org/10.1016/j.corsci.2019.04.016.

[42] D. Wallinder, J. Pan, C. Leygraf, et al., EIS and XPS study of surface modification of 316LVM stainless steel after passivation, Corrosion Sci. 41 (1998) 275–289, https://doi.org/10.1016/S0010-938X(98)00122-X.

[43] F. Mohammadi, T. Nickchi, M.M. Attar, et al., EIS study of potentiostatically formed passive film on 304 stainless steel, Electrochim. Acta 56 (2011) 8727–8733, https://doi.org/10.1016/j.electacta.2011.07.072.

[44] G. Lorang, M. Da Cunha Belo, A.M.P. Simões, M.G.S. Ferreira, Chemical composition of passive films on AISI 304 stainless steel, J. Electrochem. Soc. 141 (1994) 3347–3356, https://doi.org/10.1149/1.2059338.

[45] C. Olsson, D. Landolt, Passive films on stainless steels—chemistry, structure and growth, Electrochim. Acta 48 (2003) 1093–1104, https://doi.org/10.1016/S0013-4686(02)00841-1.

[46] Y. Gui, Z.J. Zheng, Y. Gao, The bi-layer structure and the higher compactness of a passive film on nanocrystalline 304 stainless steel, Thin Solid Films 599 (2016) 64–71, https://doi.org/10.1016/j.tsf.2015.12.039.

[47] D.S. Kong, S.H. Chen, C. Wang, et al., A study of the passive films on chromium by capacitance measurement, Corrosion Sci. 45 (2003) 747–758, https://doi.org/10.1016/S0010-938X(02)00148-8.

[48] N.E. Hakiki, M.D.C. Belo, A.M.P. Simoes, et al., Semiconducting properties of passive films formed on stainless steels: influence of the alloying elements, J. Electrochem. Soc. 145 (1998) 3821–3829, https://doi.org/10.1149/1.1838880.

[49] S.H. Jeon, H.J. Kim, K.H. Kong, et al., Effects of copper addition on the passivity and corrosion behavior of 27Cr-7Ni hyper duplex stainless steels in sulfuric acid solution, Mater. Trans. 56 (2015) 78–84, https://doi.org/10.2320/matertrans.M2014233.

[50] H.P. Qu, H.T. Chen, Y.P. Lang, Influence of Mn-Ni alloying elements on surface film and pitting resistance of Cr-Mn austenitic stainless steels, Construct. Build. Mater. 125 (2016) 427–437, https://doi.org/10.1016/j.conbuildmat.2016.08.059.

[51] A.E. Yaniv, J.B. Lumsden, R.W. Staehle, The composition of passive films on ferritic stainless steels, J. Electrochem. Soc. 124 (1977) 490–496, https://doi.org/10.1149/1.2133335.

[52] I. Olefjord, B. Brox, U. Jelvestam, Surface composition of stainless steels during anodic dissolution and passivation studied by ESCA, J. Electrochem. Soc. 132 (1985) 2854–2861, https://doi.org/10.1149/1.2113683.

[53] B.B. Li, Y.P. Lang, H.T. Chen, et al., Studies on the Cooperative influence of Cr and Mo on the pitting corrosion resistance of super austenitic stainless steels, Materials 16 (2023) 7397, https://doi.org/10.3390/ma16237397.

[54] G. Latha, N. Rajendran, S. Rajeswari, Influence of alloying elements on the corrosion performance of alloy 33 and alloy 24 in seawater, J. Mater. Eng. Perform. 6 (1997) 743–748, https://doi.org/10.1007/s11665-997-0076-2.

[55] H. Baba, Y. Katada, Effect of nitrogen on crevice corrosion in austenitic stainless steel, Corrosion Sci. 48 (2006) 2510–2524, https://doi.org/10.1016/j.corsci.2005.09.010.

[56] I. Olefjord, L. Wegrelius, The influence of nitrogen on the passivation of stainless steels, Corrosion Sci. 38 (1996) 1203–1220, https://doi.org/10.1016/0010-938X(96)00018-2.

[57] L. Freire, M.A. Catarino, M.I. Godinho, et al., Electrochemical and analytical investigation of passive films formed on stainless steels in alkaline media, Cem. Concr. Compos. 34 (2012) 1075–1081, https://doi.org/10.1016/j.cemconcomp.2012.06.002.

[58] H. Sun, X.Q. Wu, E.H. Han, Effects of temperature on the oxide film properties of 304 stainless steel in high temperature lithium borate buffer solution, Corrosion Sci. 51 (2009) 2840–2847, https://doi.org/10.1016/j.corsci.2009.08.006.

[59] S.E. Ziemniak, M.E. Jones, K.E.S. Combs, Solubility and phase behavior of Cr(III) oxides in alkaline media at elevated temperatures, J. Solut. Chem. 27 (1998) 33–66, https://doi.org/10.1023/A:1022688528380.

[60] R. Kirchheim, B. Heine, H. Fischmeister, et al., The passivity of iron-chromium alloys, Corrosion Sci. 29 (1989) 899–917, https://doi.org/10.1016/0010-938X(89)90060-7.

[61] M. Kuczynska-Wydorska, I. Flis-Kabulska, J. Flis, Corrosion of low-temperature nitrided molybdenum-bearing stainless steels, Corrosion Sci. 53 (2011) 1762–1769, https://doi.org/10.1016/J.CORSCI.2011.01.054.

[62] V. Maurice, W.P. Yang, P. Marcus, X-Ray photoelectron spectroscopy and scanning tunneling microscopy study of passive films formed on (100) Fe-18Cr-13Ni single-crystal surfaces, J. Electrochem. Soc. 145 (1998) 909–920, https://doi.org/10.1149/1.1838366.

[63] B.B. Li, Y.P. Lang, H.T. Chen, et al., Studies on the Cooperative Influence of Cr and Mo on the Pitting Corrosion Resistance in Super Austenitic Stainless Steels, Materials. 16(1023) 7397, https://doi.org/10.3390/ma16237397.

[64] H. Luo, C.F. Dong, Characterization of passive film on 2205 duplex stainless steel in sodium thiosulphate solution, Appl. Surf. Sci. 258 (2011) 631–639, https://doi.org/10.1016/j.apsusc.2011.06.077.

[65] L. Chen, C.M. Shi, X.L. Li, et al., Passivation of hydrogen damage using graphene coating on α-Fe$_2$O$_3$ films, Carbon 130 (2018) 19–24, https://doi.org/10.1016/j.carbon.2017.12.119.

[66] M. Liu, Y. Jin, C. Zhang, et al., Density-functional theory investigation of Al pitting corrosion in electrolyte containing chloride ions, Appl. Surf. Sci. 357 (2015) 2028–2038, https://doi.org/10.1016/J.APSUSC.2015.09.180.